Tomographic reconstruction of shallow water bubble fields

Daniel Rouseff, *Senior Member*, and Frank S. Henyey

Applied Physics Laboratory, College of Ocean and Fishery Sciences,

University of Washington, 1013 NE 40th Street, Seattle, WA 98105.

Jerald R. Caruthers and Stephen J. Stanic

Naval Research Laboratory, Ocean Acoustics Branch,

Stennis Space Center, MS 39529.

Abstract

In the winter of 1997, a shallow water experiment was conducted near the Scripps Pier in La Jolla, California, USA. The goal was to determine the dynamics, distribution and acoustic effects of bubbles just offshore from active surf. A major component of the experiment was the "Delta Frame," an apparatus that supported two acoustic sources and eight receivers. Acoustic intensity was measured at frequencies between 39 and 244 kHz over the resulting 16 horizontal ray paths. Paths ranged in length from 2.5 to 8.6 m. In the present paper, a tomography algorithm is developed and implemented using Delta Frame data. Measurements are combined to produce quantitative cross-sectional images of the attenuation associated with the bubble cloud. Numerical simulations predict that the frame can resolve details of the field down to about 2 m. Images constructed at different acoustic frequencies are scaled and compared. A five-minute sequence of images is studied in detail. Swell waves are shown to cause rapid fluctuations in the images due to the vertical structure of the bubble cloud. At a wave trough, the bubble cloud dips into the horizontal plane probed by the Delta Frame and the attenuation increases.

Introduction

Bubbles, even in small concentrations, have strong effects on underwater acoustic propagation. They produce strong attenuation, and they change the sound speed. Unlike most acoustic environments, bubble clouds cause the sound to be strongly dispersed. As a crude approximation useful to guide one's thinking, the complex index of refraction at any frequency depends on the bubbles that resonate at that frequency, and the resonant frequency is inversely proportional to the radius of the bubble. The processes that remove bubbles from the water determine the index of refraction as a function of frequency. Large bubbles rapidly rise to the surface, and small bubbles dissolve, leaving intermediate size bubbles to dominate the acoustic effects.

Because of the strong dispersion, a transmitted pulse shape is greatly distorted if it propagates a significant distance through a bubble cloud. Under such conditions, the very definition of a travel time becomes uncertain. It turns out to be much easier to interpret intensity measurements in terms of attenuation rather than travel times. The real part of the index of refraction is better studied by short-range phase velocity measurements than by transmission (group) speeds. Another consequence of the strong dispersion is that measurements at different frequencies give independent information about the bubble clouds.

Near the ocean shore, bubbles produced by surf are often the dominant complication in acoustic propagation. These bubbles are transported by nearshore currents. Rip currents carry them offshore, and may affect attempts to use acoustics probes near the shore. An experiment to determine the dynamics, distributions, and acoustic effects of bubbles in shallow water just offshore from active surf was conducted from 24 February to 14 March, 1997. The region of interest was just north of the pier at the Scripps Institution of Oceanography. The region extended from a few tens of meters to a thousand meters from the beach. Efforts were made to acquire a comprehensive data set of coastal dynamics, bubble distributions, and acoustic propagation using a variety of techniques [1-5]. A major emphasis was placed on a smaller region approximately 400 m^2 in area and about 300 m offshore, where most of the instruments were clustered.

The dynamics of rip currents at the Scripps Pier have been discussed in a number of papers [6-8]. An earlier sector-scan sonar study of rips at the SIO pier found clear evidence of rip currents and described their character which includes strong acoustic backscatter [8]. That study suggested that the backscatter is due to microbubbles rather than the sediment load they also carry, but could not confirm the speculation. The bubble content of rip events was reported to be one of their least understood characteristics. A sector-scan sonar used during the Scripps Pier Bubble Experiment also observed the acoustic backscattering [3]. A preponderance of evidence collected by the participants established the fact that backscattering is due to microbubbles [1-5,9,10].

An important component of the1997 experiment was the Delta Frame. The frame supported two sources and eight hydrophones. Intensity (interpreted by attenuation) and timing (to try to extract travel time) measurements were made along the resulting sixteen intersecting paths at eight frequencies between 39 and 244 kHz. This frequency range spanned the resonant frequencies of bubbles thought to be present. Note that individual transmission measurements represent intrinsically averaged quantities. The logarithm of intensity (i.e., the signal level in dB), for example, is reduced by attenuation integrated over the entire acoustic path. In order to recover details of the field smaller than the path length, it is necessary to combine measurements taken along different paths. Tomography is a systematic way to combine data and produce quantitative cross-sectional pictures of the medium.

In this paper, a tomography algorithm is first derived and then applied to the Delta Frame measurements. Features of the bubble field between 2 and 10 m in size are imaged. The images show how the bubble field responds to ensonification at different acoustic frequencies and how the field evolves in time. Modulation of the bubble field by local surface waves is observed.

In Section 1, relevant details of the Delta Frame measurements are discussed. Section 2 begins with a derivation of the tomography algorithm. The algorithm is then implemented and tested in numerical simulations to estimate the resolution that can be expected. The algorithm is applied to the Delta Frame data in Section 3. The frequency dependence of attenuation is examined. A sequence of images sampling the bubble field every second is presented. Finally, the results are discussed in Section 4.

I. Delta Frame Measurements

The Delta Frame was deployed approximately 12 m north of the Scripps Pier near piling 33. The outer frame was in the shape of a triangle with each leg approximately 9.4 m long. Figure 1 is a top view showing the location of the two acoustic sources labeled A and B at vertices of the triangle. The eight numbered receivers are distributed around the outer frame. Also shown are the resulting 16 intersecting ray paths that range in length from 2.5 to 8.6 m. Legs 1.6 m in length supported the frame. To avoid spurious reflections, extenders supported the sources and receivers above the frame boosting the acoustic paths to 2.8 m above the seabed in water nominally 4.3 m deep. A weak prevailing current to the south insured that effects of the pier pilings did not contaminate the bubble fields at the frame. The sources had narrow beampatterns in the vertical directions to further reduce the effects of scattering from the frame and to eliminate scattering from the surface and bottom.

Measurements along the paths were made at eight frequencies: 39, 59, 78, 98, 117, 146, 186, and 244 kHz. Each frequency component had a 0.1 ms duration, with a modified Hanning envelope. The frequency components and the sequence of their emissions were specially coded to insure that the various components did not overlap at any hydrophone and that all transmissions would occur within a 12 ms period to fit into an active ping schedule including emissions from other experiments. The received signals were sampled at 625 kHz in 12 bits. The cycle of eight transmissions from each of the two sources were made once a second for an hour and a half, this constituting a Run. Over the course of ten days, ten runs were made.

The conditions that prevailed for most of Run 6 provided a very stable baseline of signals. For Source A the standard deviation of the signal level was less than 0.02 dB and for Source B less than 0.05 dB during quiescent periods. Over the course of the ten days of measurements, numerous periods occurred that matched the data of Run 6 within 0.1 dB (equating to errors of less than 0.05 dB/m) and no period occurred in which data exceeded the data of Run 6 by more than the expected

error. Consequently, averaging ten pings in Run 6 beginning with Sequence 0200 establishes a valid "zero-bubble" baseline. This baseline calibrates the "no loss" case and, unless otherwise noted, all values of loss are referenced to it.

These small variations in transmission properties are to be compared to the attenuation due to bubbles that were determined to be 5 to 30 dB when rip events prevailed. Generally these events were more prevalent during low tide when surf breaking was just shoreward of the frame. The remainder of this work will discuss these variations in attenuation.

II. Tomographic Inversion Algorithm

It is not practical to image individual bubbles. Rather, the goal of the inversion is to determine the effective index of refraction produced by an aggregate of bubbles. The effective index of refraction is complex having a real part related to the speed of sound and an imaginary part related to attenuation. In the following, the inversion algorithm is derived. The algorithm is then implemented and tested in numerical simulations to estimate the resolution of the imaging system.

2.a Theory

Let $\alpha(\mathbf{r})$ represent the spatially varying attenuation associated with the bubble field in a horizontal plane $\mathbf{r} = (x, y)$. Sound is transmitted through the bubble field from several different directions within the plane. Taking the negative of the logarithm of the intensity measured along path i yields the datum d_i modeled by

$$d_i = \int \alpha(\mathbf{r}_i) d\eta_i + \varepsilon_i. \tag{1}$$

The vector $\mathbf{r}_i$ is constrained to lie along the ray path, $d\eta_i$ is the increment along the path, and ε_i is the noise. In the present application, the ray path is assumed to be straight connecting the source and receiver. It is assumed that N such measurements are available probing the medium from different directions. The problem reduces to estimating the unknown two-dimensional function $\alpha(\mathbf{r})$ from N measured projection integrals.

The reconstruction of a function from its projections is a classic problem with wide application in many fields. In a medical CT scanner, for example, upwards of one million projections are measured and used to generate an image [11]. In such cases, well-known techniques based on the Radon transform can be applied. These methods build essentially no assumptions about the field into the inversion algorithm; the large number of measurements obviates the need for a priori information. In the present application, N equals only 16 and an alternative inversion approach is required.

The recent monograph by Munk et al. offers a comprehensive review of ocean acoustic tomography [12]. Given a limited number of measurements, the most common approach is to parameterize the medium. This is the so-called discrete-data/discrete-solution approach. The medium is divided into layers or cells and the goal of the inversion is to estimate the associated parameters. In the present application, the medium is not segmented; rather, a discrete-data/continuous-solution is sought. This approach is more commonly used in geophysics. The continuous-solution method produces an image that is smooth and consistent with the assumed statistical nature of the bubble field.

An estimate $\hat{\alpha}(\mathbf{r})$ for the attenuation field is sought in the form

$$\hat{\alpha}(\mathbf{r}) = \sum_{i=1}^{N} g_i(\mathbf{r}) d_i, \tag{2}$$

where the functions $g_i(\mathbf{r})$ are to be determined. Equation (2) produces an estimate that is linearly dependent on the data.

There are several ways to derive essentially equivalent inversion algorithms. Often the discussion couched in terms of the Gauss-Markov method [12]. The resulting image is interpreted as a realization of a random process. In the present case, some of the requirements of the Gauss-Markov model, specifically that both the field $\alpha(\mathbf{r})$ and the noise be realizations of Gaussian processes, need not be satisfied. Only when they are Gaussian, though, does (2) give the optimum image in the least-squares sense. What is required is that both the field and the noise have known autocorrelation functions and that the processes are uncorrelated with each other. Although not necessary, for simplicity in the development it is further assumed that the field is statistically homogeneous and isotropic. Using angle brackets to denote an ensemble average, the autocorrelation of the attenuation field is defined by

$$\langle \alpha(\mathbf{r})\alpha(\mathbf{r}') \rangle = R(|\mathbf{r} - \mathbf{r}'|). \tag{3}$$

Define the objective function J from the difference between the true field and its estimate:

$$J = \left\langle [\alpha(\mathbf{r}) - \hat{\alpha}(\mathbf{r})]^2 \right\rangle. \tag{4}$$

The functions $g_i(\mathbf{r})$ are found by minimizing (4). Let $\mathbf{g}$ and $\mathbf{d}$ be column vectors with elements g_i and d_i, respectively. Substituting (2) into (4) and differentiating gives

$$\frac{\partial J}{\partial \mathbf{g}} = -\left\langle 2\left[\alpha(\mathbf{r}) - \mathbf{g}^T(\mathbf{r})\mathbf{d}\right]\mathbf{d}^T \right\rangle. \tag{5}$$

Equating to zero and solving yields

$$\mathbf{g}^T(\mathbf{r}) = \left\langle \alpha(\mathbf{r})\mathbf{d}^T \right\rangle \cdot \left\langle \mathbf{d}\mathbf{d}^T \right\rangle^{-1}. \tag{6}$$

The uncorrelated nature of the field and the noise, together with (1), permits the ensemble averages in (6) to be calculated:

$$\psi_i(\mathbf{r}) \equiv \left\langle \alpha(\mathbf{r})d_i \right\rangle = \int R(|\mathbf{r} - \mathbf{r}_i|)d\eta_i, \tag{7}$$

$$\left\langle \mathbf{d}\mathbf{d}^T \right\rangle = \mathbf{M} + \mathbf{V}, \tag{8}$$

where $\mathbf{M}$ is the "influence matrix" describing the correlation between pairs of measurements. It has elements

$$M_{ij} = \iint R(|\mathbf{r}_i - \mathbf{r}_j|)d\eta_i d\eta_j, \tag{9}$$

and $\mathbf{V}$ describes the noise correlation with elements $V_{ij} = \left\langle \varepsilon_i \varepsilon_j \right\rangle$.

Using (6)-(9), the inversion algorithm can be rewritten in a more useful form

$$\hat{\alpha}(\mathbf{r}) = \sum_i q_i \psi_i(\mathbf{r}), \tag{10}$$

where the weights

$$\mathbf{q} = (\mathbf{M} + \mathbf{V})^{-1}\mathbf{d}. \tag{11}$$

A simple interpretation can be attached to the inversion algorithm (10)-(11). In the measurement (forward) problem, data are taken along discrete ray paths. Implicitly, each ray is of infinitesimal width. The functions $\psi_i(\mathbf{r})$ are defined as the backprojection rays used in the reconstruction (inverse) problem. From its definition (7), each $\psi_i(\mathbf{r})$ represents the corresponding original ray path in the forward problem convolved with the autocorrelation of the medium. Data taken along isolated rays in the forward problem, then, are backprojected over a smeared region in the inverse problem. The precise nature of this smearing depends upon the assumed correlation function of the underlying medium that is being reconstructed. The i-th backprojection ray is weighted by the associated q_i. The weighted backprojection rays are then superimposed via (10) to

yield a continuous reconstruction. The result is analogous to the well known filtered backprojection method used when there is continuous data [11].

Consider the computational burden associated with implementing the inversion algorithm. Elements in the $N \times N$ symmetric influence matrix $\mathbf{M}$ are found by calculating two-dimensional integrals. For realistic configurations, these integrals will likely need to be calculated numerically. Note, however, that $\mathbf{M}$ is independent of the measurements; it, as well as the inverse of $(\mathbf{M} + \mathbf{V})$, need be calculated only once even if new data $\mathbf{d}$ are measured. Similarly, each $\psi_i(\mathbf{r})$ is independent of the data. Consequently, all of the computationally expensive work can be completed prior to making any measurements. As new measurements are made, either at a later time or at a different acoustic frequency, new coefficients are found by the simple matrix multiplication in (11). The new coefficients are applied to the precalculated backprojection rays $\psi_i(\mathbf{r})$ and combined via (10) to yield the new image. Although it was not implemented during the Scripps Pier experiment, there is clearly the potential to do nearly real time imaging.

2.b Implementation

To evaluate the integrals in (7) and (9), it is convenient to define a rotated coordinate system:

$$\begin{aligned} \xi &= x\cos\theta_i + y\sin\theta_i \\ \eta &= -x\sin\theta_i + y\cos\theta_i \end{aligned}$$

(12)

In the (ξ, η) coordinates, the ray path lies parallel to the η-axis, displaced by the distance ξ_i (Figure 2). The source is at η_s, the receiver at η_r. Equation (7) becomes

$$\psi_i(\mathbf{r}) = \int_{\eta_s}^{\eta_r} R\big([(\xi - \xi_i)^2 + (\eta - \eta_i)^2]^{1/2}\big)d\eta_i .$$

(13)

It has been assumed in the derivation that the autocorrelation of the field is known. Because the true autocorrelation function is not known in practice, a functional form must be selected largely on the basis of an a priori guess as to the shape of the bubble cloud. After the reconstruction is completed, the parameters of the assumed function can be varied to confirm that the image is not unduly sensitive to the initial choice. It is also desirable that the candidate correlation function has convenient mathematical properties. Accordingly, a Gaussian correlation function is selected:

$$R(|\mathbf{r} - \mathbf{r}'|) = \exp(-|\mathbf{r} - \mathbf{r}'|^2 / L_g^2),$$

(14)

where L_g is the correlation length and is the single free parameter of the model. Substituting (14) into (13) yields

$$\psi_i(\mathbf{r}) = \sqrt{\pi} L_g \exp[-(\xi - \xi_i)^2 / L_g^2] W(\eta; \eta_r, \eta_s), \tag{15}$$

where the remaining integral

$$W(\eta; \eta_r, \eta_s) = (\sqrt{\pi} L_g)^{-1} \int_{\eta_s}^{\eta_r} \exp[-(\eta - \eta_i)^2 / L_g^2] d\eta_i$$

$$= \frac{1}{2} \left\{ \text{erf}[(\eta_r - \eta)/L_g] + \text{erf}[(\eta - \eta_s)/L_g] \right\}, \tag{16}$$

is evaluated in terms of error functions. Note that the backprojection ray is centered about the original at $\xi = \xi_i$. The width is determined by L_g. Along the direction of propagation, the properties are dictated by (16). Let $L = \eta_r - \eta_s$ be the length of the original ray. Figure 3 shows $W(\eta; L/2, -L/2)$ for various ratios of the path length to the correlation length. When $L \gg L_g$, $W \approx 1$ over most of the path, falling to 1/2 at the source and receiver locations, and then rapidly to zero. As the ratio is decreased, the backprojection ray becomes more smeared.

A final detail on the implementation: from Fig. 1, it is apparent that the difference between measurements on path A2 and A1 should equal the difference between measurements on path B1 and B2 to within the experimental error. This redundancy was used to preprocess the data and reduce the dimensionality of the inversion.

2.c. Numerical Simulations

To better understand the properties of the reconstruction algorithm before applying it to the experimental data, a series of numerical simulations were performed. In this section, results from these simulations are summarized.

A realization of a two-dimensional random process can be synthesized by first generating white noise and then filtering according to the desired spectrum. The technique is conveniently implemented using fast Fourier transforms. Figure 4(a) shows a 10 m by 10 m patch consistent with a Gaussian spectrum. The correlation length is $L_g = 2.5 \, \text{m}$. Superimposed on the realization is the outline of the Delta Frame. Not shown are the $N=16$ ray paths connecting the two sources and eight receivers supported by the frame. Using two-dimensional interpolation and a simple quadrature scheme, the projection integrals along the 16 paths can be calculated. This serves as the data that can be input to the inversion algorithm. Figure 4(b) shows the resulting reconstruction. Over the interior of the Delta Frame, the results are quite satisfactory as all the essential features of

the original are recovered in the reconstruction. Interestingly, there is also reasonable agreement around the periphery of the frame; it is possible to extrapolate to a distance nearly L_g outside of the frame. This is due to where the sources and receivers are positioned on the frame and because the finite correlation length of the medium is known. As one would expect, no information about the field far outside of the frame can be gleaned.

Simulations of the type shown in Fig. 4 were repeated for various values of L_g. To quantify the inversion quality, the difference between the original and the reconstruction was calculated on a pixel-by-pixel basis. This error was then squared and averaged over the interior of the delta frame. The root mean square error was normalized so that if the original and the reconstruction were uncorrelated the error would be one. Perfect agreement would result in zero error. Figure 5 shows the normalized rms error plotted versus the correlation length. As one would expect, when the correlation length is large the error is small. When the correlation length becomes less than about 2 m, the error increases rapidly. Physically, this means that there are not enough ray paths to recover the detailed structure in a medium with scale sizes less than a few meters.

III. Reconstruction of the Bubble Field

In this section, the tomographic inversion algorithm is applied to attenuation measurements made during the Scripps Pier experiment. All the images are oriented to be consistent with the geometry shown in Fig. 1. The effect of varying the assumed correlation length, the lone free parameter of the inversion algorithm, is studied. The frequency dependence of attenuation is demonstrated. An extended sequence of images is generated showing the temporal evolution of the bubble field.

Recall that each transmission sequence consisted of eight frequencies and was repeated every second. As a labeling convention, sequence number is equivalent to time in seconds since the start of a run. There were ten runs at Scripps Pier Experiment, each lasting approximately 90 minutes. Results in this section concentrate on Run 5 which began 7 March, 1997 at 13:58:20 local time, and Run 7 which began 14:23:32 on 8 March. Run 5 is of particular interest since this is both a period of high activity and a time when other investigators were making independent measurements of the bubble field.

3.a Effect of varying the correlation length

Figure 6(a) shows a sample bubble field reconstruction from Run 7. The 59 kHz measurements were averaged over ten seconds beginning 2823 seconds into Run 7. A correlation length $L_g = 2.5$ m was assumed. The spatially varying nature of the medium is apparent; a swath of relatively high attenuation, 7 dB/m, is visible over the interior of the frame.

As formulated, the single free parameter in the inversion algorithm is the correlation length L_g. Reducing the assuming correlation length reduces the overlap between pairs of

backprojection rays (7) and forces the off-diagonal terms in the influence matrix (9) to shrink. The value for L_g was varied to test the effect on the inversion. Figure 6(b) is generated using the same data as Fig. 6(a) but assumes $L_g = 1.0$ m. Reducing the correlation length has made the image more fragmented as it becomes concentrated in the areas where the rays passed in the forward problem. Still, the difference between the two images is not too great; regions of high attenuation are located at the same place and are of essentially the same level.

There are trade-offs in selecting the assumed correlation length. Choosing a short correlation length reduces the residual error between the measurement and the least-squares fit, but at the expense of a fragmented image like Fig. 6(b). Choosing a correlation length that is too large, however, can introduce oscillations in the image. This is illustrated in Fig. 7 using data from sequence 3159 of Run 5. Figure 7(a) shows the reconstruction using the 146 kHz measurements and $L_g = 2.5$ m. A region where the attenuation takes a significantly negative value is apparent. This non-physical result can be corrected by reducing the correlation length. In Fig. 7(b), $L_g = 0.5$ m was assumed. Now a small region of high attenuation is seen occupying the space between Source A and Receiver 3. There is essentially no other activity in the image space and the reconstruction goes only slightly negative. Clearly, this is a situation where using our formulas with a long correlation length is not justified.

Obtaining negative values for the reconstructed attenuation serves as a useful diagnostic in assessing the plausibility of an image. Slightly negative regions, as in Fig. 6, are accepted as an intrinsic feature of the inversion procedure and not corrected. For aberrant situations, as in Fig. 7(a), the correlation length is reduced and a new image generated. Unless otherwise noted, $L_g = 2.5$ m is assumed.

3.b. Effect of varying the acoustic frequency

The predominant mechanism for attenuation in bubble fields is resonant scattering. With the Delta Frame, each sequence consisted of eight frequencies allowing bubbles of different sizes to be probed synoptically. Consequently, for each sequence, up to eight tomographic images can be generated. These images show how attenuation varies with acoustic frequency, but also how different sized bubbles are distributed spatially.

Figure 8 shows bubble field attenuation images for acoustic frequencies from 39 to 244 kHz. The projection data have been averaged over ten seconds starting from sequence 2823 of Run 7. Comparing the images, the most attenuation occurs at 59 kHz. Using the orientation defined in Fig. 1, the 59 kHz image shows a localized region of high attenuation reaching 7 dB/m located between receivers 1 and 2. A broad swath of comparable level stretches over the body of the frame. At higher frequencies, the basic shape of the bubble field does not appear to change significantly, but the level of attenuation is reduced.

Figure 8 demonstrates the strong frequency dependence of attenuation. It is difficult, however, to compare the images; a color bar appropriate for 59 kHz has too much dynamic range for 244 kHz. To better compare the results, it would be useful to have a model for the functional dependence of attenuation on frequency. From this model, the images could be rescaled and compared using a common color bar. The frequency dependence of attenuation remains a subject of active research. In the present context, an empirical scaling can be derived from the images in Fig. 8. For a particular image $\hat{\alpha}(\mathbf{r})$, define the frame-averaged attenuation

$$\overline{\alpha} = \int \hat{\alpha}(\mathbf{r})d\mathbf{r} \tag{17}$$

where the integration is over the triangle bounded by the Delta Frame. Figure 9 shows $\overline{\alpha}$ calculated for each frame in Fig. 8 and plotted versus frequency. The maximum is at 59 kHz. Define the frequency-scaled image at a particular frequency:

$$(scaled\ image) = \left(\frac{\overline{\alpha}(59\,\mathrm{kHz})}{\overline{\alpha}(f)} \right) \times (old\ image).$$

The proposed scaling was applied to the images in Fig. 8 with the results shown in Fig. 10.

Several observations can be made from Fig. 10. First, the scaling is reasonable up to 186 kHz; the first seven images essentially "fit" on the same color scale. A more telling point is that the first seven images shown look remarkably similar to one another. Under the assumption of resonant scattering, recall that large bubbles are sensitive to low frequencies while small bubbles respond to high frequencies. The similarity of the images implies that in this instance the bubble distribution is nearly homogeneous; the small bubbles responding to 186 kHz sound are not located in a different region than the large bubbles resonating at 39 kHz.

The proposed scaling does, however, begin to fail at the highest frequency. The 244 kHz image actually has a maximum of 16 dB/m and a minimum of -4 dB/m causing it to saturate at both ends of the color scale. Note, however, that the location of the maxima is generally consistent with what was observed in all the other images. As in the previous section, decreasing the correlation length would reduce the overshoot in the image. It is unclear if the anomalous behavior at 244 kHz is a genuine effect or an artifact. The relatively low attenuation at the highest frequency suggests a possible problem separating the signal from noise, or errors in defining the background attenuation level. Additional comments on the frequency dependence of the reconstructions are presented in the following section.

3.c Reconstruction of an extended time-series

A five-minute portion from Run 5 beginning with sequence 3050 was chosen for detailed analysis. Figure 11 shows the 146 kHz attenuation field averaged over the frame. For the first part of the time series, the average attenuation is less than 1 dB/m. Beginning around 3180 seconds, the average attenuation generally increases to sequence 3250, then falls over the next 40 seconds. A more rapid oscillation is superimposed on these broad characteristics. The attenuation is negligible from 3300 to 3349 s. This time period was used to correct for biases in the individual paths and to estimate the noise correlation matrix $\mathbf{V}$ in (8).

Also shown in Fig. 11 is the average attenuation at 244 kHz. As expected, the average attenuation is less than was observed at 146 kHz. Note that the two time series generally track one another.

During the period of maximum activity, some paths were so strongly attenuated as to be unmeasureable for frequencies less than 146 kHz. Consequently, the imaging concentrated on the 146 kHz measurements. With a suitable model for the frequency dependence, these images could presumably be scaled to predict attenuation characteristics at other frequencies.

Figure 12 shows a ten second sequence of images starting at 3250 s. No attempt was made to do any time averaging of the data; each frame was reconstructed in isolation. Certain features appear persistent across the images. Referring to Fig. 1 for the location of the sources and receivers, the broad feature extending from source A to receiver 5 is apparent. The peak level associated with the feature, however, varies from frame-to-frame.

A possible cause of the variability in the images is wave motion. To test this conjecture, Fig. 13 shows $\overline{\alpha}(t)$, the attenuation averaged over the frame for the two minutes of maximum activity. Superimposed on the plot is the local water depth as measured by a pressure sensor located near source A [13]. Comparing the two plots, attenuation maxima correspond to wave troughs while attenuation minima correspond to wave crests.

To quantify the apparent relationship between attenuation and surface height, a correlation analysis was performed. Figure 14 shows the average attenuation $\overline{\alpha}(t)$ and a low-pass filtered version $\overline{\alpha}_{LP}(t)$ of the time-series. The proposed model is that the observed $\overline{\alpha}(t)$ is a slowly varying function modulated by the surface height $h(t)$. To test the model, the linear correlation coefficient r between the ratio $\overline{\alpha}(t)/\overline{\alpha}_{LP}(t)$ and $h(t)$ was calculated. Setting $\overline{\alpha}(t)>1$ dB/m as a threshold for model validity, $r=-0.75$ resulted. For a 2 dB/m threshold, $r=-0.86$. This strong anti-correlation confirms that for this section of data the temporal variability is dominated by vertical motion of the swell waves. The Delta Frame measures a two-dimensional, mostly horizontal, structure. As a result, the vertical motion cannot be followed directly; we just see bubbles disappear from the plane as the crest of the wave approaches, and return as the trough approaches. During this period of high attenuation, horizontal advection of the bubble field is expected, but it is masked by these wave effects.

IV. Summary

The Delta Frame was designed to measure spatial and temporal structure of bubble clouds in a rip current. When this experiment was being planned, there was little information on the spatial scales of variability in the bubble clouds. The experiment was designed to measure variability on scales between 2 m and 10 m. This was a fortunate choice, because the tomographic reconstructions show structure throughout this range. Our reconstructed images show that there is significant variation over 2 m; possibly there are actual scales smaller than the resolution of the delta frame. On occasion, it appears that structure smaller than the resolution occurs; setting the correlation length to 1m removes the large negative bubble density from the image. On the other hand, there are structures in our images that extend considerably more than 2 m in one direction.

The delta frame measures the bubble field in one horizontal plane. There is major vertical structure that is made apparent by the vertical advection from the swell waves. This advective effect dominates the temporal variability in the Delta Frame plane. At a wave trough, the bubble cloud dips into the horizontal plane probed by the Delta Frame and the attenuation increases. At a wave crest, the cloud rises and attenuation decreases. These wave effects tend to mask the horizontal advection of the bubble cloud.

The discrete-data/continuous-solution tomography algorithm we chose proves useful. The reconstructed images do not have discrete cells in which the field is assumed constant; rather, the structure of the independent functions composing the images are set by the geometry of the experiment and by the assumed correlation scale. In the algorithm we use, it is possible to carry out sensitivity studies and to change parameters such as the correlation length.

References

[1] J.W. Caruthers, S.J. Stanic, and P.A. Elmore, and R.R. Goodman, "The Scripps Pier Bubble Experiment 1997 and overview of rip events and their effects on acoustic measurements," *J. Acoust. Soc. Am.*, vol.103, p. 2828, 1998.

[2] P.H. Dahl, J.W. Caruthers, and S.J. Stanic, "Vertical profiles and horizontal scales of bubble clouds in the surf zone as measured with a distributed array of upward-looking sonars," *J. Acoust. Soc. Am.*, vol.103,. p. 2828, 1998.

[3] S. Vagle and D. Farmer, "Bubble generation and dispersion in the surf zone," *J. Acoust. Soc. Am.*, vol.103,. p. 2828, 1998.

[4] E.J. Terrill and W.K. Melville, "Bubbles and surf zone oceanography," *J. Acoust. Soc. Am.*, vol.103,. p. 2828, 1998.

[5] J.W. Caruthers, S.J. Stanic, and P.A. Elmore, and R.R. Goodman, "Effects of bubbles on high-frequency sound propagation in very shallow water," *J. Acoust. Soc. Am.*, vol.103,. p. 2829, 1998.

[6] D.L. Inman and B.M. Bush, "The Coastal Challenge", *Science*, vol.181, pp. 20-32, 1973.

[7] C.D. Miller and A. Barcilon, "The Dynamics of the Littoral Zone", *Rev. Geophys.*, vol. 14, pp. 81-91, 1976.

[8] J.A. Smith and J.L. Largier, "Observations of Nearshore Circulation: Rip Currents", *J. Geophys. Res.*, vol. 100, pp 10,967-10,975, 1995.

[9] J.W. Caruthers, S.J. Stanic, and P.A. Elmore, "Acoustic attenuation in very shallow water due to the presence of bubbles in rip currents," *J. Acoust. Soc. Am.*, vol. 106, pp. 617-625, 1999.

[10] J.W. Caruthers, P.A. Elmore, J.C. Novarini, and R.R. Goodman, "An iterative approach for approximating bubble distributions from attenuation measurements," *J. Acoust. Soc. Am.*, vol. 106, pp. 185-189, 1999.

[11] A. C. Kak and M. Slaney, *Principles of Computed Tomographic Imaging*, NY: IEEE Press, 1988.

[12] W. Munk, P. Worcester and C. Wunch, *Ocean Acoustic Tomography*, Cambridge: Cambridge Press, 1995

[13] Pressure sensor data provided courtesy of P. Dahl, personal communication.

Figure captions:

Figure 1. Scale drawing of Delta Frame showing location of sources A and B and eight receivers.

Figure 2. Rotated coordinate for ray i. Source and receiver at (ξ_i, η_s) and (ξ_i, η_r), respectively.

Figure 3. Smearing function $W(\eta; \eta_r, \eta_s)$ defined by (16). Evaluated at $\eta_r = L/2$ and $\eta_s = -L/2$ where L is the path length. Plotted for various ratios of the path length to the outer scale.

Figure 4. Reconstruction simulation. (a) Original image. Realization of process with Gaussian correlation function and correlation length 2.5 m. Triangle shows location of delta frame. (b) Tomographic reconstruction. Red-green-blue color scale is arbitrary.

Figure 5. Estimating the resolution of the imaging system. Normalized error calculated by comparing original and tomographic reconstruction. Results plotted versus correlation length. Error becomes large as correlation length shrinks below a few meters.

Figure 6. Effect of choosing a correlation length on the reconstruction using experimental data. Run 7, sequence 2823, 59 kHz data with (a) L_g=2.5 m, and (b) L_g=1.0 m.

Figure 7. Effect of choosing a correlation length on the reconstruction using experimental data. Run 5, sequence 3159, 146 kHz data with (a) L_g=2.5 m, and (b) L_g=0.5 m.

Figure 8. Reconstruction of bubble field attenuation at acoustic frequencies from 39 to 244 kHz. Run 7, sequence 2823.

Figure 9. Average attenuation versus frequency for sequence 2823 of Run 7. Calculated applying Eq. (17) to images in Fig. 8.

Figure 10. Scaled reconstruction of bubble field attenuation at acoustic frequencies from 39 to 146 kHz. Run 7, sequence 2823.

Figure 11. Five minute sequence of attenuation images averaged over area of Delta Frame. Both 146 and 244 kHz data used. Time in seconds relative to start of Run 5.

Figure 12: Ten second sequence of reconstructions. Time in seconds after start of Run 5. 146 kHz data used to generate images.

Figure 13: Comparison of reconstructed attenuation averaged over frame and measurement of local water depth. Peaks in attenuation correspond to troughs in surface waves. Averaged attenuation derived from146 kHz data and time relative to start of Run 5.

Figure 14. Attenuation images averaged over frame compared to lowpass version of data. Ratio of curves used in text to construct model for effects of swell waves. Time relative to start of Run 5.
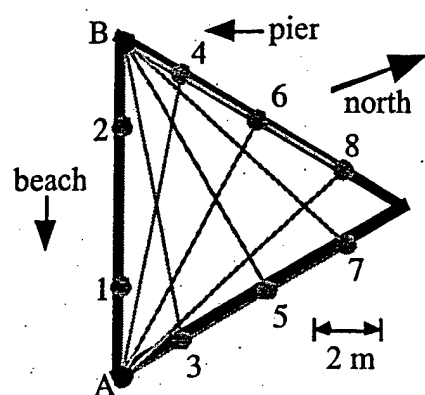
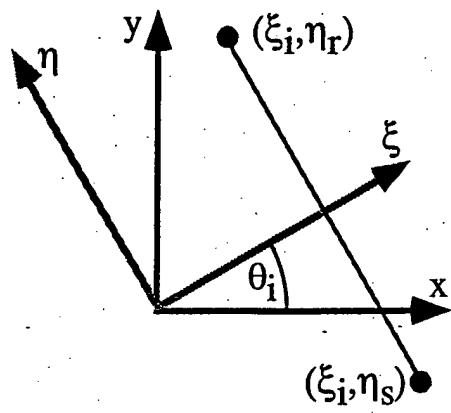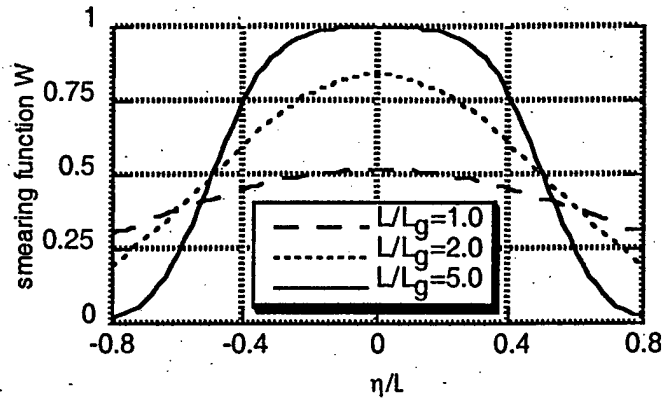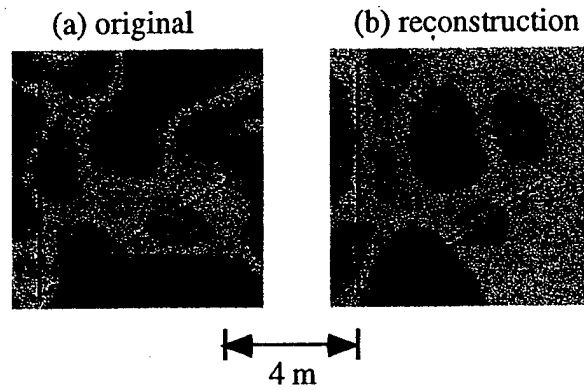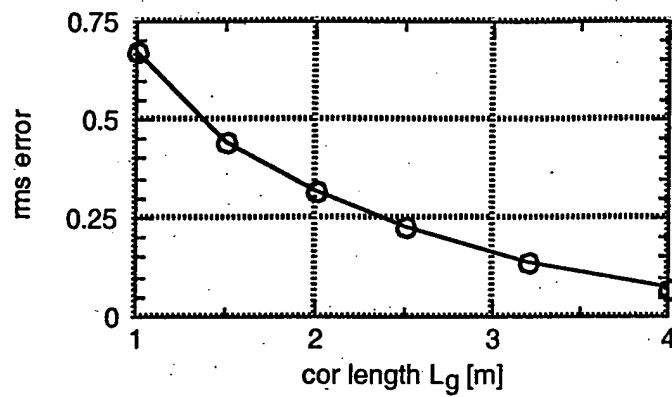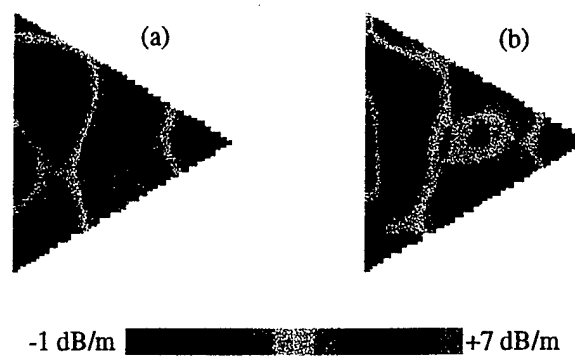Figure 1. Scale drawing of Delta Frame showing location of sources A and B and eight receivers.

Figure 2. Rotated coordinate for ray i. Source and receiver at (ξ_i, η_s) and (ξ_i, η_r), respectively.

Figure 3. Smearing function $W(\eta; \eta_r, \eta_s)$ defined by (17). Evaluated at $\eta_r = L/2$ and $\eta_s = -L/2$ where L is the path length. Plotted for various ratios of the path length to the outer scale.

(a) original   (b) reconstruction

4 m

Figure 4. Reconstruction simulation. (a) Original image. Realization of process with Gaussian correlation function and correlation length 2.5 m. Triangle shows location of delta frame. (b) Tomographic reconstruction. Red-green-blue color scale is arbitrary.

Figure 5: Estimating the resolution of the imaging system. Normalized error calculated by comparing original and tomographic reconstruction. Results plotted versus correlation length. Error becomes large as correlation length shrinks below a few meters.

Figure 6. Effect of choosing a correlation length on the reconstruction using experimental data. Run 7, sequence 2823, 59 kHz data with (a) L_g=2.5 m, and (b) L_g=1.0 m.

Figure 7. Effect of choosing a correlation length on the reconstruction using experimental data. Run 5, sequence 3159, 146 kHz data with (a) L_g=2.5 m, and (b) L_g=0.5 m.
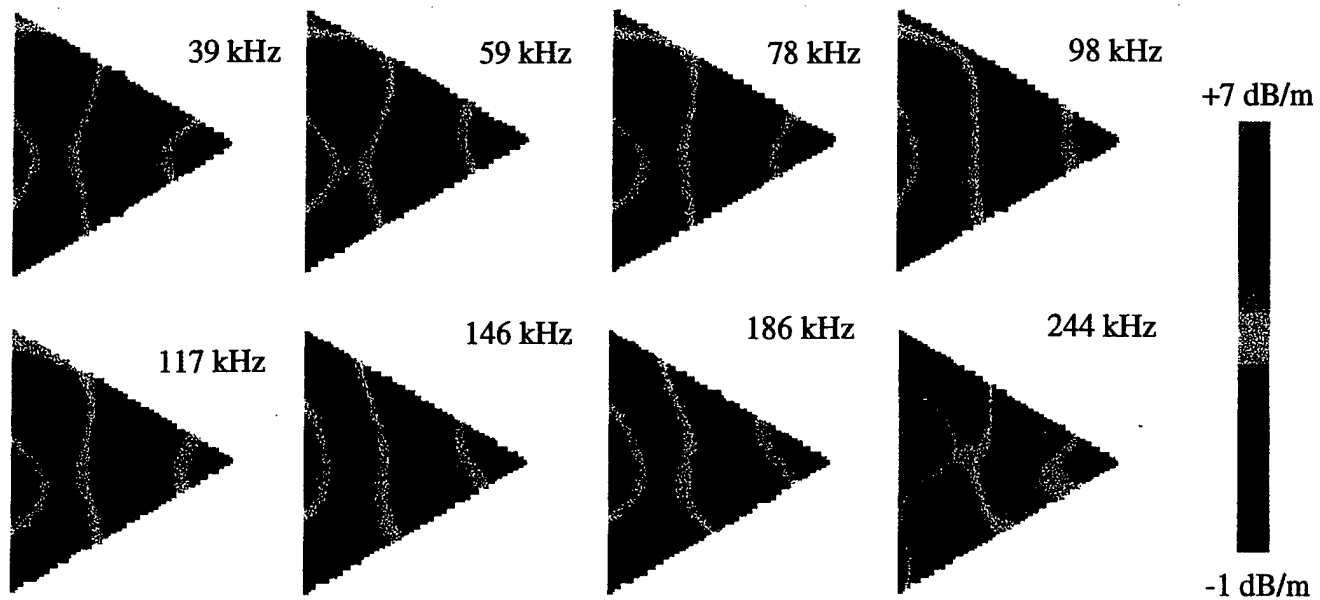
Figure 8. Reconstruction of bubble field attenuation at acoustic frequencies from 39 to 244 kHz. Run 7, sequence 2823.

Figure 9. Average attenuation versus frequency for sequence 2823 of Run 7. Calculated by applying Eq. (17) to images in Fig. 8.

Figure 10. Scaled reconstruction of bubble field attenuation at acoustic frequencies from 39 to 146 kHz. Run 7, sequence 2823.
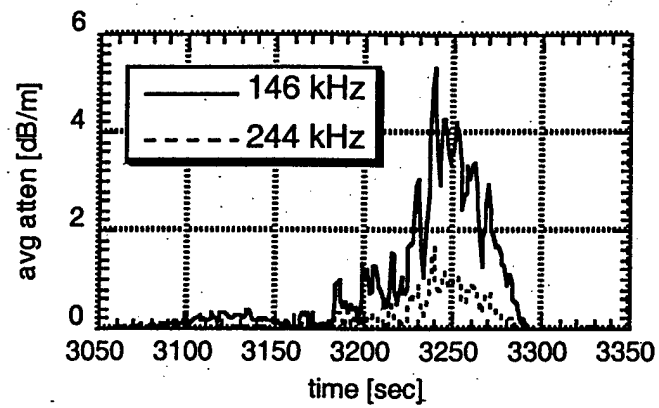
Figure 11. Five minute sequence of attenuation images averaged over area of Delta Frame. Both 146 and 244 kHz data used. Time in seconds relative to start of Run 5.
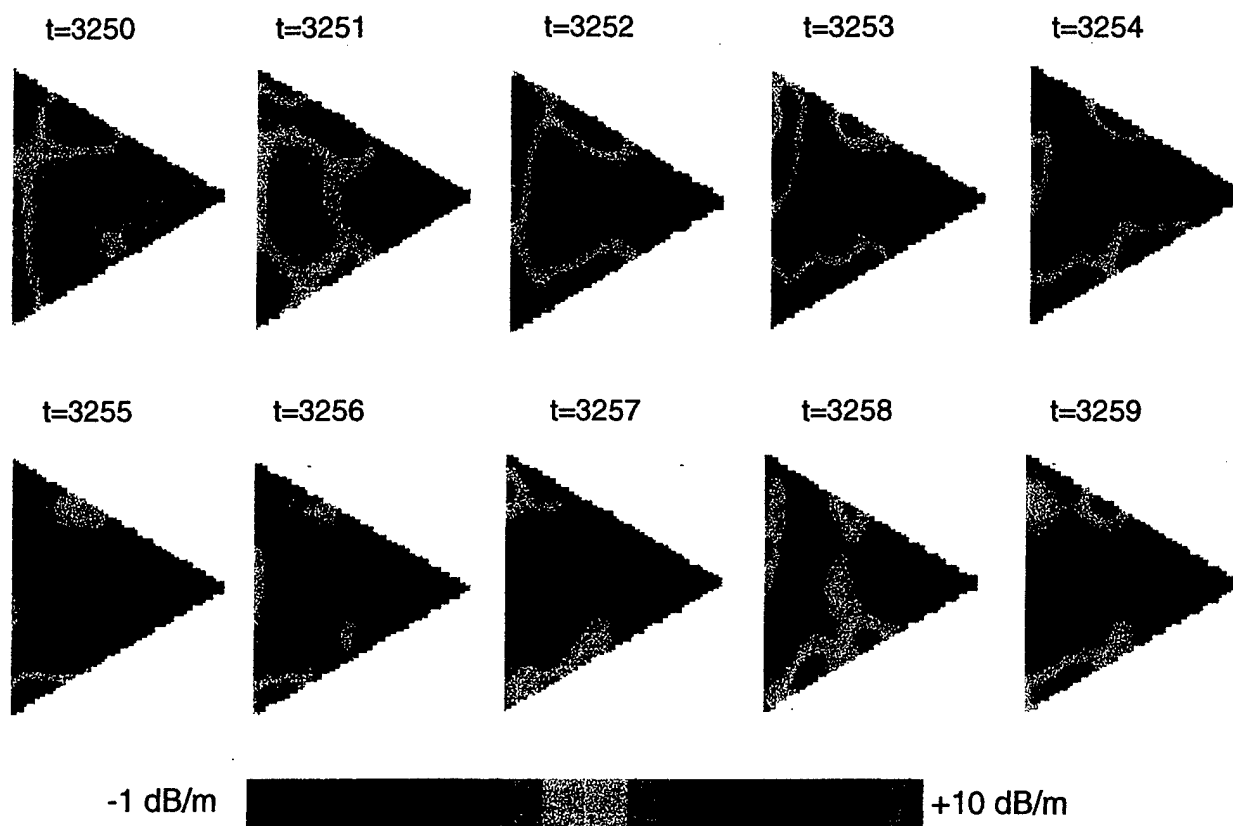
t=3250　　t=3251　　t=3252　　t=3253　　t=3254

t=3255　　t=3256　　t=3257　　t=3258　　t=3259

-1 dB/m　　　　　　　　　　　　　　　　　　+10 dB/m

Figure 12: Ten second sequence of reconstructions. Time in seconds after start of Run 5. 146 kHz data used to generate images.
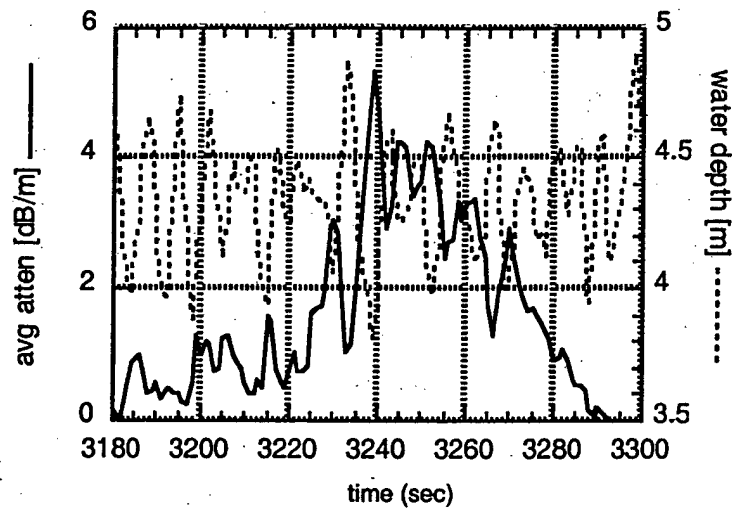
Figure 13: Comparison of reconstructed attenuation averaged over frame and measurement of local water depth. Peaks in attenuation correspond to troughs in surface waves. Averaged attenuation derived from146 kHz data and time relative to start of Run 5.
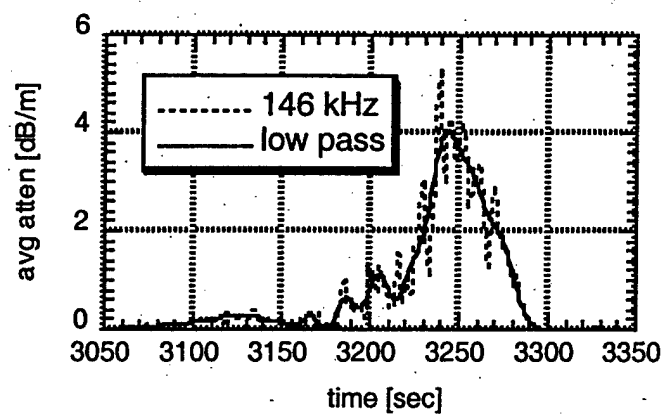
Figure 14. Attenuation images averaged over frame compared to lowpass version of data. Ratio of curves used in text to construct model for effects of swell waves. Time relative to start of Run 5.